Sensors & Actuators: B. Chemical 443 (2025) 138210



Contents lists available at ScienceDirect

Sensors and Actuators: B. Chemical

journal homepage: www.elsevier.com/locate/snb





Core morphology effect of Pd-Au_{NR}@ZnO core-shell nanoparticles on hydrogen gas sensing properties

Tuong Van Tran [a], Dong-Seog Kim [a], Geun-Jae Oh [a], Ho-Geun Song [b], Dae-Hee Won [c,*], Yeon-Tae Yu [a,*]

[a] Division of Advanced Materials Engineering, Research Center for Advanced Materials Development, Jeonbuk National University, Jeonju 54896, Republic of Korea
[b] Ogam Technology, Jangseong 57247, Republic of Korea
[c] Division of Liberal Art, Wonkwang University, Iksan 54538, Republic of Korea

ARTICLE INFO

Keywords:
Pd-Au alloy
Nanorod
ZnO
Core-shell
Hydrogen gas sensor

ABSTRACT

In this study, the Pd@Au core-shell nanorod (CS-NR) with Au shell thickness of about 3 nm is first prepared and then the $Zn(OH)_2$ nanoparticle (NP) outer shell is covered over the Pd@Au CS-NR core by the hydrothermal method. It is noteworthy that the Pd@Au_{NR}@$Zn(OH)_2$ double CS-NPs are transformed into Pd-Au_{NR}@ZnO CS-NPs with nanorod-shaped Pd-Au alloy cores after calcination at 500ºC. The Pd-Au_{NR}@ZnO sensor exhibits higher hydrogen sensitivity than Au_{NR}@ZnO and pure ZnO sensors. Indeed, the Pd-Au_{NR}@ZnO sensor shows a higher response (105) for 100 ppm of hydrogen at 250ºC. Additionally, in comparison to Au_{NR}@ZnO and pure ZnO sensors, the Pd-Au_{NR}@ZnO sensor presents quicker response and recovery times. Moreover, it is found that the Pd-Au_{NR}@ZnO sensor can detect a hydrogen concentration down to 1 ppm at low temperature (150ºC). Furthermore, this sensor demonstrates a much greater selectivity for hydrogen gas than other target gases such as acetaldehyde, ethanol, methane, and carbon monoxide. These enhancements could be ascribed to the core morphology, electronic sensitization, and hydrogen absorption effect of the Pd-Au alloy nanorod-shaped core.

1. Introduction

Hydrogen, an odorless and colorless gas, is promising as a substitute fuel for our future energy demands [1–3]. Nevertheless, because hydrogen is very flammable, it is crucial to find any leaks and accurately measure the concentration of hydrogen in fuel cell systems during the whole hydrogen manufacturing, transportation, and storage process [4–9].

There are currently numerous types of hydrogen sensors, including metal oxide semiconductor, electrochemical, catalytic, optical thermo-electric, and acoustic wave sensors [10,11]. Metal oxide semiconductor (MOS) is among the most promising materials for hydrogen gas sensing due to their low cost, long-term stability, and good mobility [12–16]. Alternatively, zinc oxide (ZnO), an n-type semiconductor, is a highly suitable material for hydrogen gas detection because of its high electron mobility, non-toxicity, chemical/thermal stability, and incredibly numerous nanostructures [17–22]. However, it has the disadvantages of high working temperature and low selectivity to hydrogen gas [23–28].

In addition, the palladium (Pd) noble metal is regarded as the ideal option for hydrogen sensing because of its ability to absorb hydrogen molecules [29–34]. However, Pd nanoparticles deposited on the surface of semiconductor materials have several drawbacks, including their easy oxidation and agglomeration under high working temperatures during practical operation [35–39]. While alloying Pd catalyst with Au can improve hydrogen gas sensing in MOS gas sensors due to its anti-oxidation effect and form Pd-Au@MOS core@shell structure to protect Pd from agglomeration [40–43]. In our previous study, we successfully fabricated Pd-$Au_{nanosphere}$@ZnO core-shell nanoparticles (Pd-Au_{NS}@ZnO CS-NPs) with a gradient composition Pd-Au alloy core. The Pd-Au_{NS}@ZnO CS-NPs sensor had a high response for hydrogen gas, but the optimum operating temperature was still high at 300 °C [44]. In addition to using precious metals as catalysts, the material morphology has an impact on the performance of gas sensors since it is associated with the sensing layer's carrier transport property [45–50]. However, the research conducted in this area is very limited work. Therefore, this research focuses on the gas sensor performance according to the Pd-Au

* Corresponding authors.
E-mail addresses: trantuong12194@gmail.com (T. Van Tran), dongseogkim1019@gmail.com (D.-S. Kim), oh1340@naver.com (G.-J. Oh), ogamnara@daum.net (H.-G. Song), oneday@wku.ac.kr (D.-H. Won), yeontae@jbnu.ac.kr (Y.-T. Yu).

https://doi.org/10.1016/j.snb.2025.138210
Received 28 March 2025; Received in revised form 25 June 2025; Accepted 26 June 2025
Available online 27 June 2025
0925-4005/© 2025 Elsevier B.V. All rights are reserved, including those for text and data mining, AI training, and similar technologies.

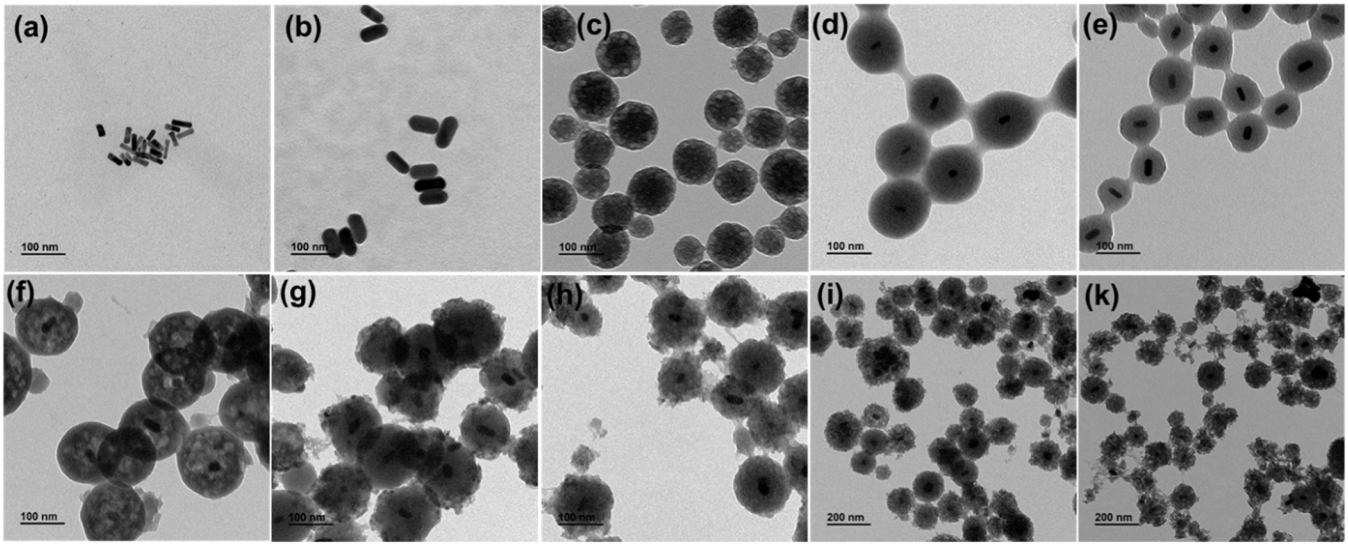


Fig. 1. TEM images of (a) Pd NRs, (b) Pd@Au CS-NRs, (c) $Zn(OH)_2$ NPs, (d) $Au_{NR}@Zn(OH)_2$ CS-NPs, (e) $Pd@Au_{NR}@Zn(OH)_2$ double CS-NPs. (f-k) as-calcined $Pd@Au_{NR}@Zn(OH)_2$ double CS-NPs with different temperatures: (f) 100ºC, (g) 200ºC, (h) 300ºC, (i) 400ºC, and (k) 500ºC.

alloy core morphology at low operating temperatures.

In this study, the $Pd@Au_{NR}@Zn(OH)_2$ double CS-NPs were prepared via a hydrothermal method, and heat-treated at various temperatures (100–500 °C) to obtain Pd-Au_{NR}@ZnO CS-NPs, and the morphological change of the nanorod (NR) core due to heat were observed. The role of the nanorod-shaped Pd-Au alloy core formed after calcination on gas sensing performances was tested by comparing the response of as-calcined Au_{NR}@ZnO CS-NPs and pure ZnO NPs. The gas sensing mechanism of the as-calcined Pd-Au_{NR}@ZnO CS-NPs for hydrogen gas was discussed in detail.

2. Experimental section

2.1. Materials

Poly(vinyl pyrrolidone) (PVP, $M_W \approx 55{,}000$), hexadecyltrimethylammonium bromide (CTAB, $C_{19}H_{42}BrN$, 99 %), sodium tetrachloropalladate (II) (Na_2PdCl_4, 98 %), potassium iodide (KI, 99 %), ascorbic acid ($C_6H_8O_6$, 99 %), zinc nitrate hexahydrate ($Zn(NO_3)_2{\cdot}6H_2O$, 98 %), and hexamethylenetetramine (HMTA, $C_6H_{12}N_4$, 99 %) were purchased from Sigma Aldrich; ethylene glycol (EG, $C_2H_6O_2$, 99 %) were purchased from Showa Chemicals Co., Ltd.; and hydrogen tetrachloroaurate (III) hydrate ($HAuCl_4.3.7H_2O$, 99.99 %) was purchased from Kojima Chemicals Co., Ltd.

2.2. Synthesis of Pd NRs

Firstly, 29.4 mg Na_2PdCl_4 was dissolved in 20 mL of distilled water, then adding 300 mg KI and 1 g PVP with vigorously stirring at room temperature. Secondly, the resulting mixture was transferred to a 100 mL stainless-steel autoclave with a Teflon vessel and heated at 200ºC for 4 h. Then, the products were collected through centrifugation at 10,000 rpm for 20 min and washed three times with ethanol-acetone (2:1) to remove surfactants. Finally, the final precipitates of Pd NRs were dispersed in 5 mL distilled water for subsequent usage.

2.3. Synthesis of Pd@Au CS-NRs and Pd-Au_{NR}@ZnO CS-NPs

To prepare Pd@Au CS-NRs, Pd NRs (1 mL, 20 mM) were dispersed uniformly in 20 mL EG. The mixed solution was transformed into a 50 mL three-neck round-bottom flask connected to a condenser and heated at 50 °C for 30 min with magnetic stirring. Then, $HAuCl_4$ (1 mL, 10 mM) was added to this solution to form Pd@Au CS-NRs. The resultant solution was kept at 50 °C for 10 h. The product was collected by centrifugation at 10,000 rpm for 20 min and washed twice with ethanol-acetone (2:1), then washed twice with the distilled water.

Pd-Au_{NR}@ZnO CS-NPs were fabricated using a hydrothermal method. CTAB (4 mL, 100 mM) was added into a 100 mL glass vial containing 50 mL of the distilled water with magnetic stirring. Then, 5 mL of Pd@Au colloid was added. Next, ascorbic acid (2 mL, 100 mM), $Zn(NO_3)_2{\cdot}6H_2O$ (2 mL, 200 mM), and HMTA (2 mL, 200 mM) were also introduced to the above solution with stirred vigorously for 10 min. After that, the glass vial was carefully sealed and heated to 86 °C for 8 h in an electric oven. After the reaction was completed, the $Pd@Au_{NR}@Zn(OH)_2$ solution was centrifuged at 15,000 rpm for 20 min and washed three times with the distilled water. At last, the precipitated $Pd@Au_{NR}@Zn(OH)_2$ double CS-NPs were dried at 60 °C for 24 h before being annealed at 500 °C for 2 h with heating rate of 1 °C/min in a muffle furnace to obtain Pd-Au_{NR}@ZnO CS-NPs.

2.4. Characterization techniques

Transmission electron microscopy (TEM) images were performed using Cs-corrected transmission electron microscope (Cs-STEM) (JEOL, JEM-2010) with an accelerating voltage of 200 kV. UV–visible spectra with a spectrophotometer (V-770, Jasco) was recorded at room temperature in the range of 300–800 nm using quartz cuvettes with a 1 cm path length and water as a reference sample. The crystal structure was measured by X-ray diffractometry (XRD; D/Max 2005, Rigaku) using CuKα radiation ($\lambda = 1.54178$ Å) at an X-ray power of 40 kV and 100 mA. The Barrett-Emmett-Teller (BET) technique (Micromeritics TriStar 3000) was utilized to present the specific surface area and average pore width. X-ray photoelectron spectroscopy (XPS) (Thermo Fisher Scientific, Multilab 2000) was performed by using monochromated Al Kα X-ray photon ($h\nu = 1486.6$ eV) sources to investigate the surface chemical states of the elements. Ultraviolet photoelectron spectroscopy (UPS) was analyzed using same XPS system with the He I line – UV source (21.2 eV). From UPS spectra, the work function (Φ) was calculated by the formula: $(\Phi) = E_{He\ I} - E_{cut\text{-}off}$ (eV).

2.5. Fabrication and measurement of gas sensing device

For gas sensing device fabrication, 20 mg of calcined Pd-Au_{NR}@ZnO material was mixed with 20 μL of α-terpineol to form a uniform paste

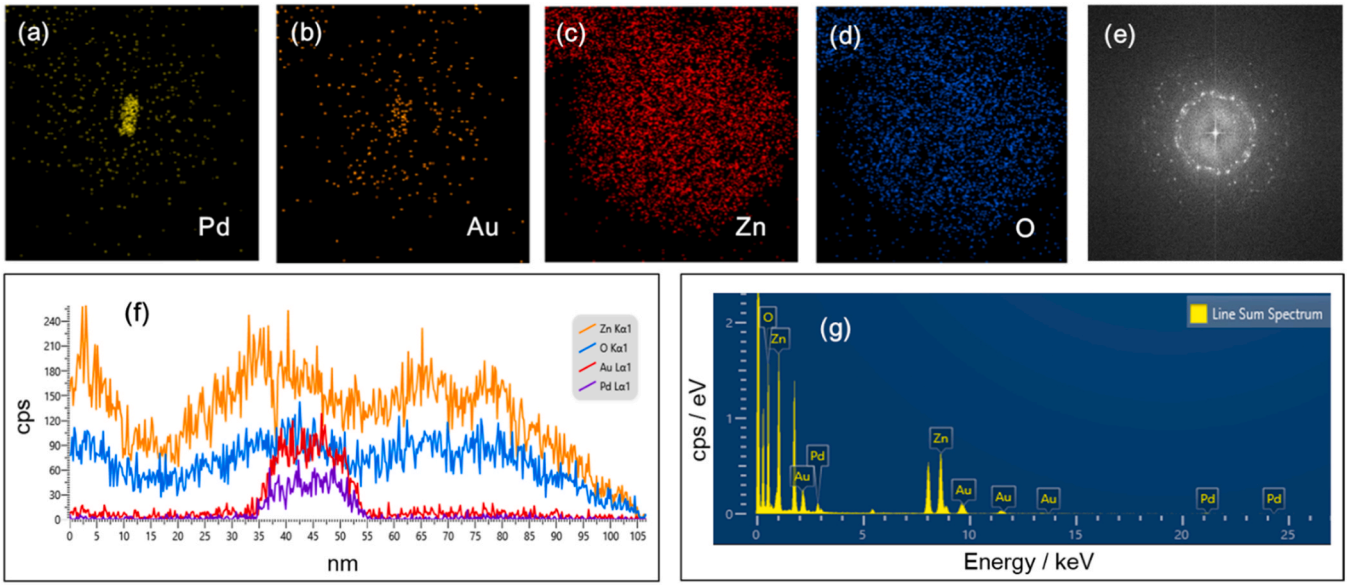


Fig. 2. (a-d) STEM-EDS results of Pd-Au_{NR}@ZnO CS-NPs with elemental maps for Pd (a); Au (b); Zn (c); O (d). (e) SAED pattern of Pd-Au_{NR}@ZnO CS-NPs. (f) corresponding EDS line scanning profiles of Pd (purple); Au (red); Zn (orange); and O (blue). The x-axis represents the distance along the line scan (nm) and the y-axis refers to the number of counts (counts per second, cps). (g) line sum spectrum of Pd-Au_{NR}@ZnO CS-NPs. The x-axis corresponds to the electron energy in kiloelectron volt (Energy / keV) and the y-axis is counts per second per electron volt (cps / eV).

and then coated on an interdigitated circuit alumina board with platinum electrodes (area = 10 mm × 10 mm, Ogam Technology Co. Ltd.). The prepared device was dried at 60 °C for 12 h in the oven, and annealed at 350 °C for 2 h with heating rate of 1 °C/min in the muffle furnace.

The gas sensing properties for the fabricated device was tested in the temperature range from 150 to 350 °C. The sensor device was positioned in the quartz tube's middle. In a high dynamic reaction chamber, the target calibration gases (100 ppm), including hydrogen (H_2), acetaldehyde (CH_3CHO), ethanol (C_2H_5OH), methane (CH_4), and carbon monoxide (CO), was balanced with N_2 as a source gas. Meanwhile, the background gas was N_2 and dry air was mixed to be 10.5 % O_2. The gas flow rate in a mass flow controller (MFC) was maintained at 100 sccm by computer management and the oxygen content was constantly kept at 10.5 %. A high resistance meter (Agilent 34970 A) was used to record the sensor's resistance change during gas testing. The gas sensing response (R_s) was defined as R_a/R_g, where R_a was the sensor resistance in dry air and R_g was the sensor resistance in target gas. In addition, the influence of humidity on the hydrogen sensing performance of the Pd-Au_{NR}@ZnO sensor was further investigated. Humid air was generated by passing dry air through water, with the relative humidity (RH%) controlled by adjusting the air flow rate. A hygrometer was installed just before the gas mixture entered the sensing chamber to precisely verify the RH% (Fig. S1).

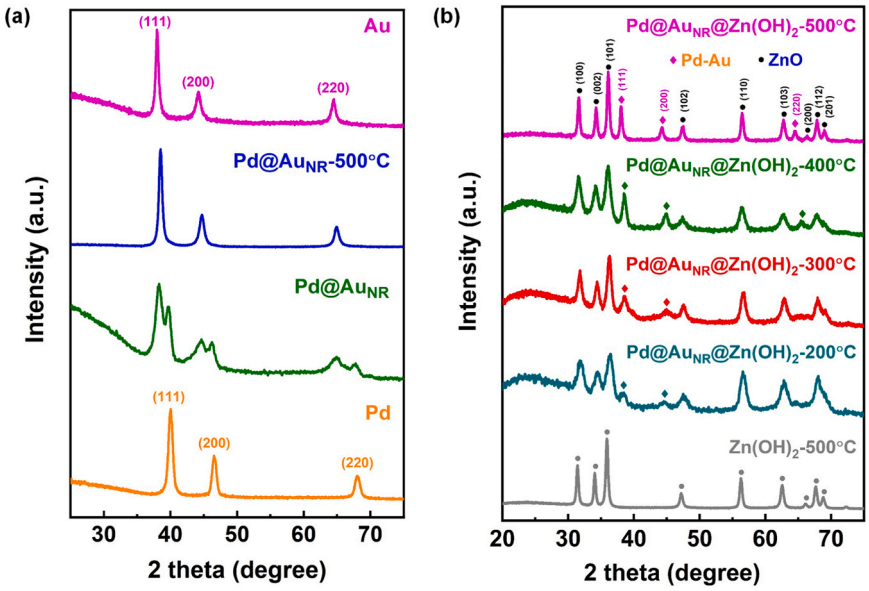


Fig. 3. XRD patterns of (a) Pd NRs, Pd@Au CS-NRs, as-calcined Pd@Au CS-NRs at 500ºC, Au NRs and (b) as-calcined $Zn(OH)_2$ NPs at 500ºC, as-calcined Pd@Au_{NR}@$Zn(OH)_2$ double CS-NPs with different temperatures: 200ºC; 300ºC; 400ºC; and 500ºC.

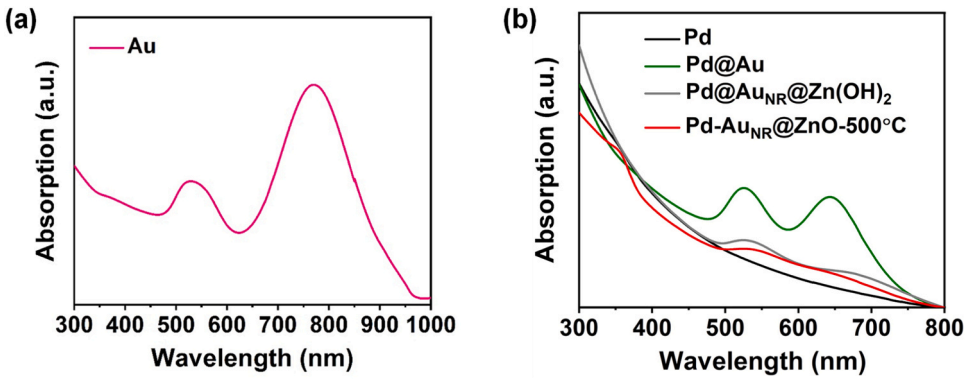


Fig. 4. UV–visible absorption spectra of (a) Au NRs and (b) Pd NRs, Pd@Au CS-NRs, Pd@Au$_{NR}$@Zn(OH)$_2$ double CS-NPs, and Pd-Au$_{NR}$@ZnO CS-NPs calcined at 500°C.

3. Results and discussion

3.1. Material characterizations

Fig. 1a shows a TEM image of Pd NRs with a uniform length and width of 40–45 nm and 10–12 nm. When Au with the thickness of about 3 nm coated on the Pd surface, the Pd@Au CS-NRs with a total particle size is increased (length: 45–50 nm, width: 12–14 nm) (Fig. 1b and S2). Spherical-shaped Zn(OH)$_2$ NPs in the range of 80–90 nm are formed as exhibited in Fig. 1c. TEM image of Au$_{NR}$@Zn(OH)$_2$ CS-NPs before calcination is shown in Fig. 1d, confirms the formation of Au$_{NR}$@Zn(OH)$_2$ CS-NPs with Au NRs encapsulated in Zn(OH)$_2$ shells. Each Au$_{NR}$@Zn(OH)$_2$ CS-NPs contains only one Au NR in the center of Zn(OH)$_2$ shell. In addition, mostly spherical-shaped Pd@Au$_{NR}$@Zn(OH)$_2$ double CS-NPs are formed, and their total sizes are from 90–100 nm. The thickness of Zn(OH)$_2$ shell in Pd@Au$_{NR}$@Zn(OH)$_2$ double CS-NPs is measured to be 45–50 nm around the Pd@Au CS-NRs (Fig. 1e). Notably, the Pd@Au CS-NRs core becomes shorter or thinner as shown in Fig. 1b, e, and S3. This phenomenon occurs because, during ZnO coating via the hydrothermal method, the chemical environment includes precursors such as Zn(NO$_3$)$_2$, ascorbic acid (AA), CTAB, and HMTA. These chemicals can be slightly oxidative or acidic/basic, potentially etching or partially dissolving the Pd@Au CS-NRs surface (e.g., CTAB-capped rods). The morphology of calcined materials is observed after heat treatment at various temperatures (100–500°C) (Fig. 1f-k and S4-S6). It can be clearly seen that the nanorod shape of Pd@Au cores is maintained up to 200°C and the shape of relatively small-sized cores is changed to sphere from 300°C. Also, the initial Pd@Au NRs are transformed into

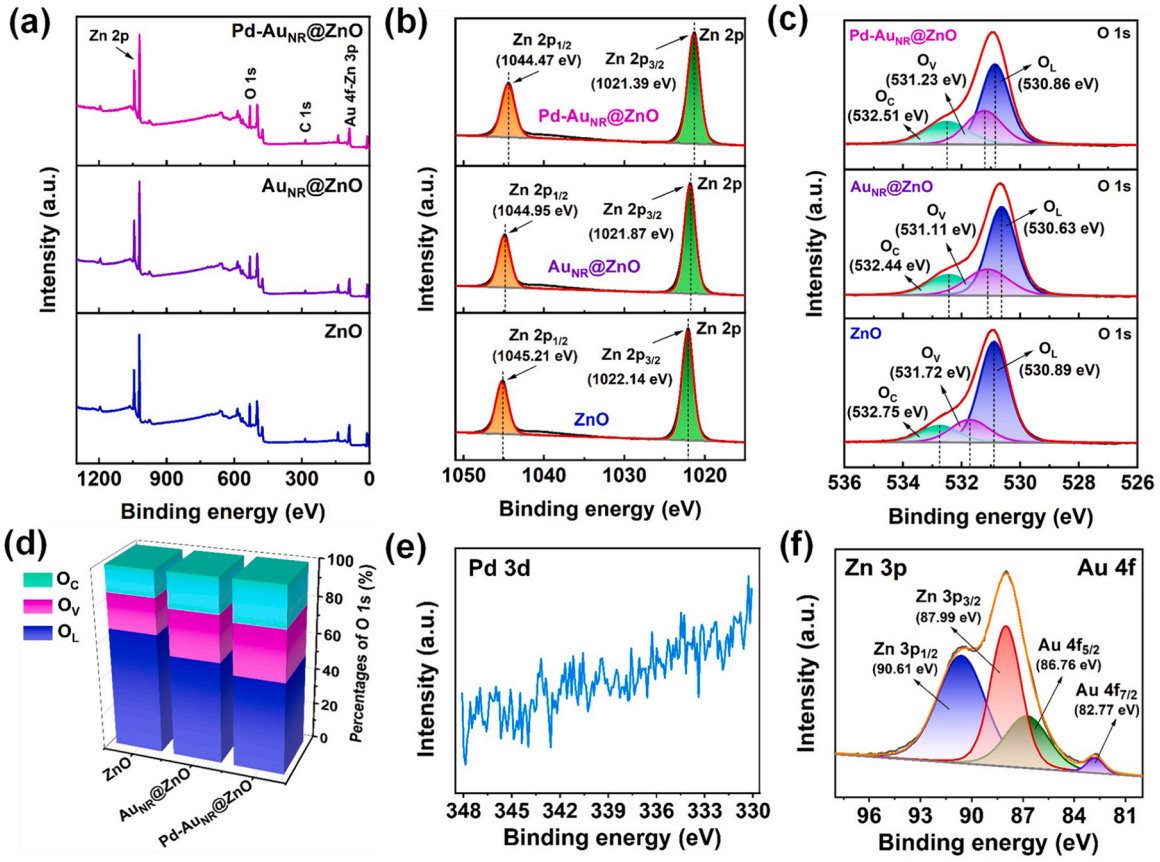


Fig. 5. (a) Full XPS survey spectra, (b) Zn 2p, (c) O 1 s, (d) percentages for various oxygen species of O 1 s in ZnO; Au$_{NR}$@ZnO; and Pd-Au$_{NR}$@ZnO, (e) Pd 3d and (f) Zn 3p–Au 4 f of the Pd-Au$_{NR}$@ZnO.

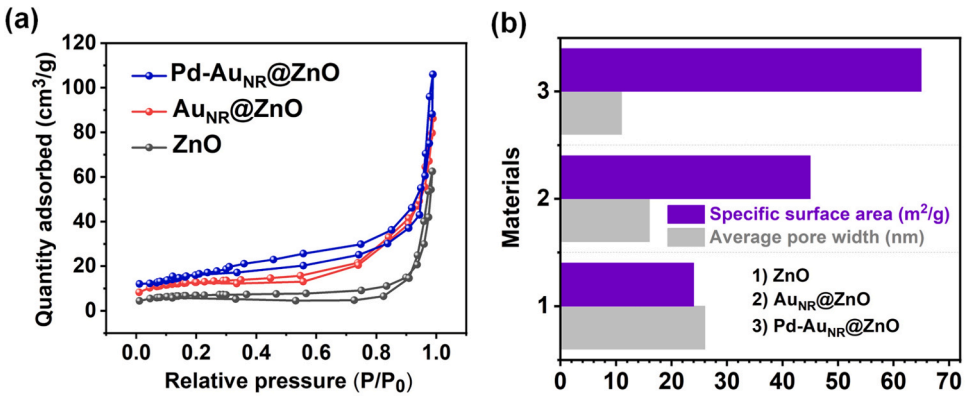


Fig. 6. (a) Nitrogen adsorption/desorption isotherm measurements and (b) corresponding average pore width contribution and specific surface area for as-calcined pure ZnO NPs, Au_{NR}@ZnO CS-NPs, and Pd-Au_{NR}@ZnO CS-NPs.

shorter and wider NRs by a gentle surface melting during heat treatment. In particular, the Pd@Au NRs length is decreased from 50 nm to 41 nm and their width is increased from 14 nm to 18 nm (Fig. 1e and h). Meanwhile, the ZnO shell becomes more crystalline and it is composed of tiny primary ZnO NPs during the calcination process.

Notably, the Pd@Au_{NR}@$Zn(OH)_2$ double CS-NPs transform to Pd-Au_{NR}@ZnO CS-NPs with different Pd-Au alloy core morphologies, including nanorod and nanosphere after calcination at 500ºC. Fig. 2a-d present the elemental mapping of Pd-Au_{NR}@ZnO CS-NPs, where the Pd and Au cores are mapped with yellow and orange colors, respectively, towards the center of particle. The distribution features of Zn and O elements in the shell are also mapped with red and blue colors, respectively. In addition, the selected area electron diffraction (SAED) pattern indicates a ring pattern, which demonstrates the formation of Pd-Au_{NR}@ZnO CS-NPs crystalline structure (Fig. 2e). Moreover, the EDS line scanning profiles for the Pd-Au_{NR}@ZnO CS-NPs are shown in Fig. 2 f, in which the orange line of the Zn and blue line of O surround the red line of the Au and purple line of Pd, reflecting the core-shell structure. From line sum spectrum result, the relative weight percent (wt%) and atomic percent (at%) ratio of Pd, Au, Zn, and O in the Pd-Au_{NR}@ZnO CS-NPs are 5.87:20.72:42.92:30.49 and 9.89:16.69:37.98:35.44, respectively (Fig. 2 g and Table S1). Besides, the elemental mapping of Pd-Au_{NS}@ZnO CS-NPs is also observed as shown in Fig. S7.

Fig. 3a describes XRD patterns of Pd NRs, Pd@Au CS-NRs, Pd-Au alloy NRs, and Au NRs. The XRD peaks are associated with the (111), (200), and (220) crystal planes of Pd NRs, and the 2θ angles of 40.04º, 46.57º, and 68.08º, respectively (JCPDS No. 46–1043). The pink line indicates that the (111), (200), and (220) crystal planes of Au NRs are represented by the 2θ angles of 37.99º, 44.26º, and 64.42º (JCPDS No. 89–3697). The XRD pattern of Pd@Au CS-NRs reveals that it is composed of Pd and Au peaks and exhibits the typical face-centered cubic (fcc) structure for each metal. Meanwhile, the XRD peaks of as-calcined Pd@Au CS-NRs are located between those of pure Pd and Au, with the 2θ angles of 38.45º, 44.76º, and 64.98º corresponding to the (111), (200), and (220), indicating that the Pd-Au alloy is formed by heat treatment at 500ºC. Hence, the as-prepared of $Zn(OH)_2$ NPs and Pd@Au_{NR}@$Zn(OH)_2$ double CS-NPs materials are calcined at different temperatures ranging from 200 to 500ºC and their XRD results are shown in Fig. 3b. From the diffraction pattern of as-calcined Pd-Au_{NR}@ZnO CS-NPs materials, a diffraction peak range from 38.2 to 38.5º is indexed to the Pd-Au alloy (111) crystal plane. Besides, the crystallinity of ZnO is greatly increased from the calcination temperature of 400ºC. The remaining peaks in all the specimens are identified as belonging to the wurtzite structure of ZnO (JCPDS No. 36–1451). No further phases or impurity peaks are found throughout the whole spectrum in the XRD analysis. As a result, the as-calcined ZnO NPs and Pd-Au_{NR}@ZnO CS-NPs are high-purity materials.

Fig. 4 shows the UV–visible absorption spectra of Au NRs, Pd NRs, Pd@Au CS-NRs, and Pd@Au_{NR}@$Zn(OH)_2$ double CS-NPs, and Pd-Au_{NR}@ZnO CS-NPs calcined at 500ºC. The Au NRs have two absorption peaks at 527 and 770 nm, corresponding to the transverse SPR (T-SPR) and longitudinal SPR (L-SPR), respectively (Fig. 4a). Meanwhile, the Pd NRs have no SPR absorption peak. In the case of Pd@Au CS-NRs, the SPR band of Au NRs shell blue-shifted to lower wavelengths of 524 nm for the T-SPR and 643 nm for the L-SPR. Following the wrapping of Pd@Au CS-NRs with loose $Zn(OH)_2$ layers, the T-SPR wavelength red-shifted to 528 nm, and the L-SPR wavelength red-shifted to 655 nm. The redshift occurs due to the higher refractive index of the surrounding medium. For the Pd-Au_{NR}@ZnO CS-NPs calcined at 500ºC, the T-SPR is successfully maintained and redshift to 537 nm. However, the L-SPR exhibits a blue-shifted to 627 nm. This result is caused by the transition of the Pd@Au CS-NRs core into a Pd-Au alloy, which is a mixture of rod and partly spherical shapes, during heat treatment at 500ºC. Moreover, the absorption peak of ZnO appears at around 355 nm, indicating that the calcined Pd-Au_{NR}@ZnO CS-NPs have outstanding absorption in the UV–visible region.

Fig. 5a shows the full XPS survey spectrum of all the materials, including pure ZnO NPs, Au_{NR}@ZnO CS-NPs, and Pd-Au_{NR}@ZnO CS-NPs, which consists of Zn 2p, O 1 s, C 1 s, and Au 4f–Zn 3p. The binding energy of C 1 s peak is used as a standard for calibration, which is located at about 285 eV. The spectrum of Zn 2p displayed two peaks with binding energies at 1045.21 eV and 1022.14 eV, which could be attributed to Zn $2p_{1/2}$ and Zn $2p_{3/2}$, confirming the existence of Zn in pristine ZnO as Zn^{2+}. Meanwhile, the Zn 2p peaks of the Au_{NR}@ZnO CS-NPs and Pd-Au_{NR}@ZnO CS-NPs materials shift towards lower binding energies compared to pure ZnO (Fig. 5b). The chemical shift implies that electrons could be transferred from the ZnO shell to the Au and Pd-Au alloy cores in the Au_{NR}@ZnO CS-NPs and Pd-Au_{NR}@ZnO CS-NPs, respectively. The above observed phenomena are associated with the difference in work function between the noble metal cores (3.94 eV for Au and 4.13 eV for Pd-Au alloy) and the ZnO shell (3.77 eV) (Fig. S10a). Since the work function of the ZnO was lower than that of the Au and Pd-Au alloy, the electrons tend to transfer from the ZnO shell to the Au and Pd-Au alloy cores [40,44,51–56]. In Fig. 5c, the binding energy of the O 1 s peak is displayed for all the materials, which are decomposed into three peaks around 530.89 eV, 531.72 eV, and 532.75 eV, corresponding to lattice oxygen species (O_L), oxygen vacancy species (O_V), and chemisorbed oxygen species (O_C), respectively (Fig. 5c). The chemisorbed oxygen species (O_C), which interacts with test gas molecules on the MOS surface, is an essential parameter for improving gas sensing performance. The percentage of O_L, O_V, and O_C for each sample is shown in Fig. 5d. The Pd-Au_{NR}@ZnO shows the maximum O_C (21.99 %) compared to other materials (Table S2). Fig. 5e shows Pd 3d spectrum of the Pd-Au_{NR}@ZnO CS-NPs. Notably, Pd characteristic peaks are not observed, as the outer layer of the Pd-Au alloy is an Au-rich alloy. The

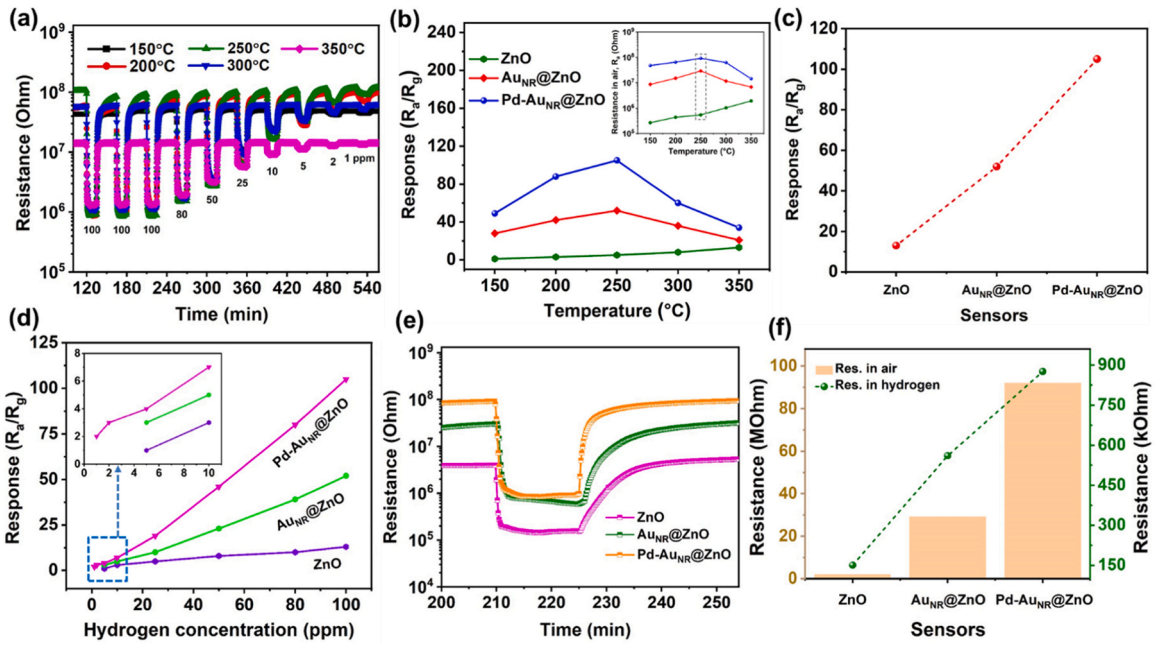


Fig. 7. Gas sensing performance for tested sensors: (a) hydrogen gas sensing activity to 100 ppm at different temperatures for Pd-Au_{NR}@ZnO sensor, (b) gas responses and baseline resistances with respect to working temperature, (c) maximal responses at optimal working temperatures, (d) sensing response in the range of 1–100 ppm hydrogen, (e) transient resistance curve, and (f) the resistance change in air and in hydrogen gas at optimal temperature for all sensors. All sensing activity measurement were conducted at optimal operating temperatures (pure ZnO; 350ºC, Au_{NR}@ZnO and Pd-Au_{NR}@ZnO sensors; 250ºC).

binding energy of the Zn 3p and Au 4 f electrons of Pd-Au_{NR}@ZnO CS-NPs are provided in Fig. 5f. The Zn 3p and Au 4 f are separated into four peaks, which correspond to Zn $3p_{1/2}$ (90.61 eV), Zn $3p_{3/2}$ (87.99 eV) of Zn^{2+} state and Au $4f_{5/2}$ (86.76 eV), Au $4f_{7/2}$ (82.77 eV) of $Au^{\delta+}$ state. In comparison to pure Au ($4f_{5/2}$, 87.71 eV and $4f_{7/2}$, 84.00 eV), the binding energy of Au 4 f is shifted to lower values [40,44, 54,57–59]. This shift is explained by the formation of negatively charged Au nanoparticles that do not form chemical bonds with ZnO.

The core-shell architecture exhibits a higher active site than the pristine MOS structure. As illustrated in Fig. 6, BET measurement is performed on the Pd-Au_{NR}@ZnO, Au_{NR}@ZnO, and pristine ZnO materials. The N_2 adsorption-desorption analysis reveals that the isothermal profiles of Pd-Au_{NR}@ZnO, Au_{NR}@ZnO, and pristine ZnO materials are identified as type IV isotherm (Fig. 6a). The specific surface area of the Pd-Au_{NR}@ZnO CS-NPs (65 m^2/g) is greater than that of the Au_{NR}@ZnO CS-NPs (45 m^2/g) and pure ZnO (24 m^2/g) (Fig. 6b and Table S3). Enhancing the active surface area of MOS materials has been proven to be an efficient strategy for improving gas sensor performances. As a

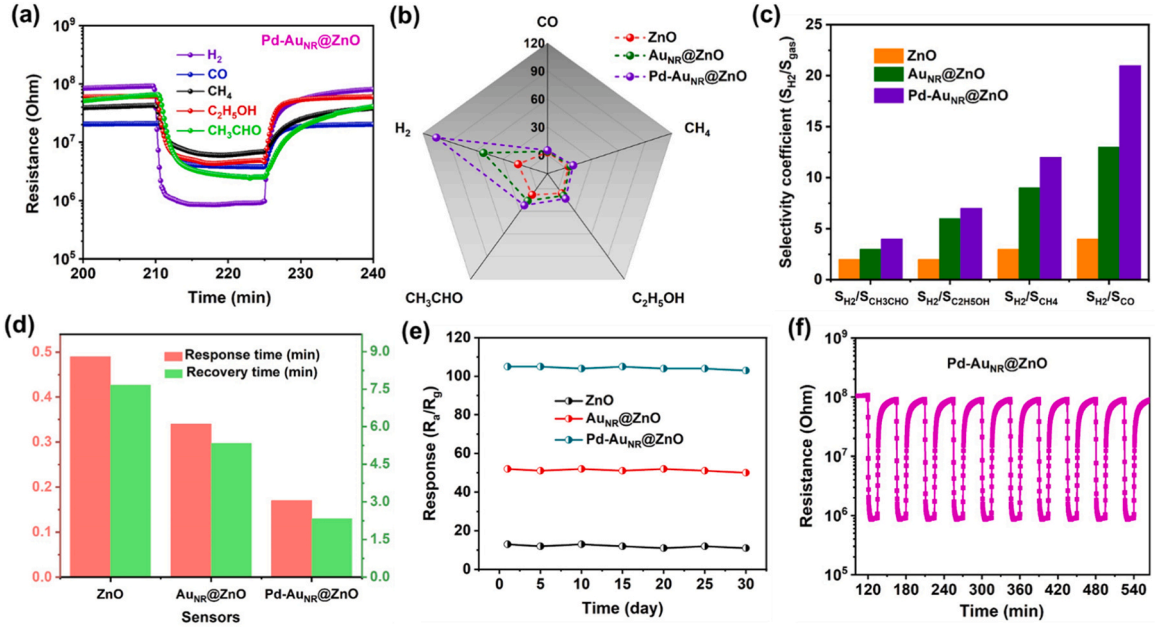


Fig. 8. Gas sensing performance for tested sensors: (a) resistance change to 100 ppm of various target gases, (b) selectivity test with 100 ppm of different target gases, (c) corresponding selectivity coefficients, (d) response and recovery times under 100 ppm hydrogen gas, (e) long-term stability of gas sensors in 100 ppm for 30 days, and (f) 10 cycles of transient response-recovery curves of Pd-Au_{NR}@ZnO to 100 ppm of hydrogen. All sensing activity measurement were conducted at optimal operating temperatures (pure ZnO; 350ºC, Au_{NR}@ZnO and Pd-Au_{NR}@ZnO sensors; 250ºC).

result, the high specific surface area of the Pd-Au_{NR}@ZnO CS-NPs increases the adsorption of hydrogen molecules, boosting gas sensing properties.

3.2. Gas sensing performances

The performance of MOS gas sensors is typically influenced by the working temperature. Therefore, it is essential to determine the optimal operating temperature for all the fabricated sensor devices. The Pd-Au_{NR}@ZnO, Au_{NR}@ZnO, and ZnO sensors are tested with 100 ppm hydrogen gas at temperatures ranging from 150 to 350 °C. The results show the typical behavior of an n-type semiconductor, which is to say that the sensor's resistance increases in the presence of air and decreases when hydrogen gas is introduced, as depicted in Fig. 7a. The response of Pd-Au_{NR}@ZnO and Au_{NR}@ZnO sensors first rises with increasing operating temperature, reaching a maximum of 250ºC for 100 ppm hydrogen. Nevertheless, the responses for both sensors rapidly decline as the working temperature is raised to 350ºC. Meanwhile, the response of pure ZnO sensor increases gradually from 150 to 350ºC (Fig. 7b and Table S4). Among the tested sensors, the Pd-Au_{NR}@ZnO CS-NPs sensor's baseline resistance value in air (R_a) is highest (92 MOhm) at 250ºC (Fig. S8 and Table S5). This result occurs due to the core morphology effect of the nanorod-shaped Pd-Au alloy core in the Pd-Au_{NR}@ZnO CS-NPs sensor. In particular, the sensor's formed chemisorbed oxygen species (O_C) percentage is maximum (21.99 %) (Fig. 5d and Table S2). As be seen in Fig. 7c, the maximal response at the optimal testing temperature of Pd-Au_{NR}@ZnO sensor ($R_s = 105$) is 2 times higher than that of Au_{NR}@ZnO sensor ($R_s = 52$) and is 8 times higher than that of ZnO sensor ($R_s = 13$) for 100 ppm of hydrogen. In addition, the responses of pure ZnO, Au_{NR}@ZnO, and Pd-Au_{NR}@ZnO sensors from low to high hydrogen concentrations (1–100 ppm) are calculated and plotted in Fig. 7d. The response values of pure ZnO, Au_{NR}@ZnO, and Pd-Au_{NR}@ZnO sensors tested for 100 ppm hydrogen gas at optimal working temperatures with different concentrations are summarized in Table S6. Remarkably, among the tested sensors, the Pd-Au_{NR}@ZnO sensor can detect a hydrogen concentration down to 1 ppm. This result indicates that the Pd-Au_{NR}@ZnO sensor is very suitable for perceiving hydrogen at low levels. The transient resistance curve of pure ZnO, Au_{NR}@ZnO, and Pd-Au_{NR}@ZnO sensors to 100 ppm hydrogen at optimal working temperature is shown in Fig. 7e. Upon exposure to a hydrogen gas environment, the resistance of all sensors decreases, and it increases again when exposed to an air atmosphere. It can be seen that the baseline electrical resistance in the air (R_a) of Pd-Au_{NR}@ZnO sensor (92 MOhm) is greatly higher as compared to that of Au_{NR}@ZnO (29 MOhm) and pure ZnO (1.9 MOhm) sensors. This is evidence of the high sensing response of the Pd-Au_{NR}@ZnO sensor to hydrogen (Fig. 7f and Table S7).

Fig. 8a-c show the selectivity of the pure ZnO, Au_{NR}@ZnO, and Pd-Au_{NR}@ZnO sensors towards interfering gases, including hydrogen (H_2), acetaldehyde (CH_3CHO), ethanol (C_2H_5OH), methane (CH_4), and carbon monoxide (CO) at the optimal working temperature. At 100 ppm, the Pd-Au_{NR}@ZnO sensor exhibits a much higher response to hydrogen (105) compared to CH_3CHO (22), C_2H_5OH (13), CH_4 (9), and CO (5), demonstrating its superior selectivity for hydrogen. The corresponding selectivity coefficients between hydrogen and other gas species for all sensors are summarized in Table S8. Response and recovery times are vital for evaluating a gas sensor's practical performance, defined as the time required for the sensor to reach 90 % of the total resistance change during adsorption and desorption, respectively. As shown in the Fig. 8d and Table S9, the Pd-Au_{NR}@ZnO sensor exhibits a quick response speed with response and recovery times of 0.17 and 2.33 min at 250ºC. Meanwhile, the response and recovery time of the Au_{NR}@ZnO and pure ZnO sensors to 100 ppm of hydrogen are relatively longer, that are 0.34 and 5.34 min at 250ºC for Au_{NR}@ZnO sensor and 0.49 and 7.67 min at 350ºC for pure ZnO sensor. It is revealed that the fast response and recovery time of Pd-Au_{NR}@ZnO CS-NPs could be ascribed to the unique Pd-Au alloy core architecture. Long-term stability for Pd-Au_{NR}@ZnO sensor is carried out for 30 days at 250ºC towards 100 ppm of hydrogen (Fig. 8e and Table S10), showing a minor decrease in response value over time. In particular, the initial response is 105, and after 30 days is 103 for the Pd-Au_{NR}@ZnO sensor. Fig. 8f and S9 present the reproducibility test of the Pd-Au_{NR}@ZnO sensor at 250ºC. The sensor's response is examined by conducting 10-cycle sensing tests toward 100 ppm hydrogen, revealing that this device maintains good reproducibility and stability during alternating exposure to air and hydrogen. Additionally, Table S11 presents a comparison of the hydrogen sensing performance of the Pd-Au_{NR}@ZnO material in this work and earlier reports.

The responses of the Pd-Au_{NR}@ZnO sensor to 100 ppm hydrogen at 250ºC were investigated under varying relative humidity (RH%) conditions of 20 %, 40 %, 60 %, and 80 %. As the RH% increases, the baseline resistance of the sensor decreases, leading to a reduction in its response to hydrogen (Fig. S13 and Table S13). This behavior can be attributed to the adsorption of water molecules on the ZnO surface in humid environments. The water molecules tend to form hydroxyl (OH^-) groups on the same active sites typically occupied by chemisorbed oxygen ions (O^-). As a result, the concentration of chemisorbed oxygen species decreases, which in turn lowers both the baseline resistance and the sensor's sensitivity to hydrogen.

3.3. Gas sensing mechanism

The sensing mechanism of an n-type semiconductor can be explained through changes in electrical resistance. Consequently, the factors that contributed to the resistance change can enhance the gas sensing properties. Upon exposure to air, a pure ZnO sensor adsorbs oxygen molecules on its surface, leading to the formation of ionic oxygen species (O_2^-, O^-, and O^{2-}).

$$O_{2\ gas} \leftrightarrow O_{2\ adsorbed} \quad (1)$$

$$O_{2\ adsorbed} + e^- \leftrightarrow O_2^- \quad (2)$$

$$O_2^- + e^- \leftrightarrow 2\ O^- \quad (3)$$

$$O^- + e^- \leftrightarrow O^{2-} \quad (4)$$

The oxygen species O_2^-, O^-, and O^{2-} are maintained at temperatures under 100ºC, 100–300ºC, and above 300ºC [60,61]. At the optimal working temperature of 350ºC, O^{2-} species are primarily generated by taking electrons from the ZnO surface. Subsequently, an electron depletion layer forms, leading to an increase in electrical resistance. Also, the generated O^{2-} species react with the target gas when introduced to the sensor, which releases electrons back to the sensing material and decreases the electrical resistance.

$$H_2 + O^{2-} \rightarrow H_2O + 2e^- \quad (5)$$

However, the pristine ZnO sensor exhibits relatively poor performance for hydrogen gas. The above result shows that the response of ZnO is 13 at 350ºC to 100 ppm hydrogen (Fig. 7b-c and Table S4). To improve the pure ZnO sensor response, Pd-Au alloy is used to design as Pd-Au_{NR}@ZnO core-shell nanostructures. For the present Pd-Au_{NR}@ZnO CS-NPs, the sensing response reaches 105 for 100 ppm hydrogen gas at a lower temperature (250ºC). The mechanism of the enhanced hydrogen sensing for Pd-Au_{NR}@ZnO CS-NPs sensor is briefly explained based on the core morphology, electronic sensitization, and hydrogen absorption properties of the Pd-Au alloy core. After calcination at 500ºC, a large number of Pd-Au_{NR}@ZnO CS-NPs with a nanorod core shaped core remained even though the Pd-Au@ZnO CS-NPs with a spherical core were partially mixed, as illustrated in Fig. 1k, 2a-d and S7. As a core morphology effect, the interface area between the ZnO shell and the nanorod-shaped Pd-Au core in the Pd-Au_{NR}@ZnO CS-NPs at the current study enhanced the sensing response at lower working temperature as compared to the Pd-Au@ZnO CS-NPs with the spherical core in previous work (Figs. S11, S12 and Table S12) [44], which increases in the oxygen

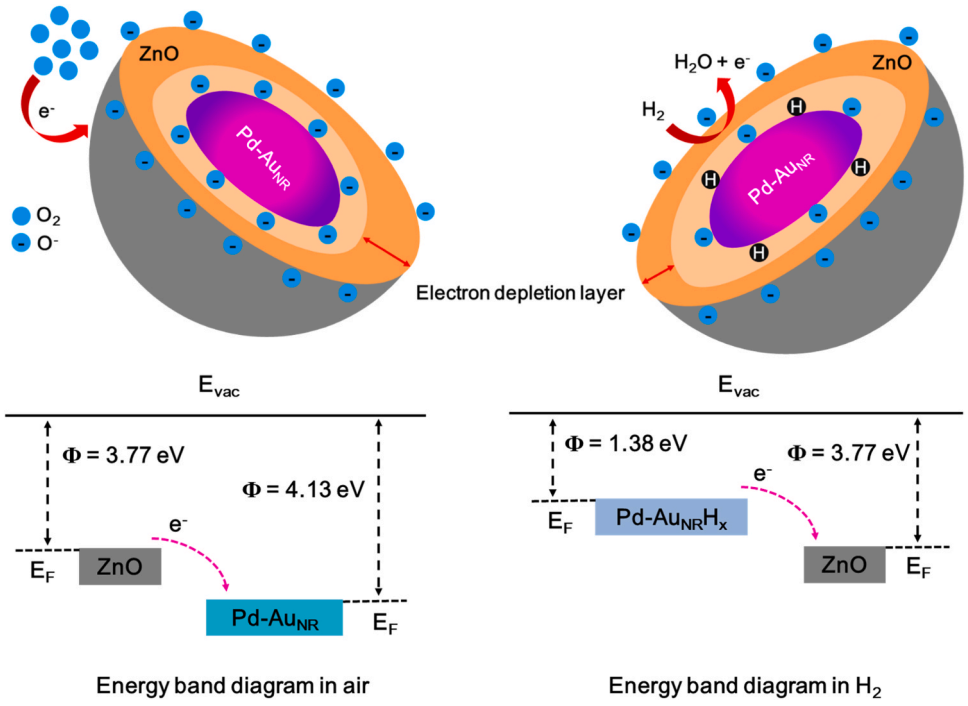


Fig. 9. Surface reaction mechanism of Pd-Au_{NR}@ZnO in air and in hydrogen.

adsorption capacity on the surface of the Pd-Au_{NR}@ZnO CS-NPs. Subsequently, a large amount of chemisorbed oxygen species is formed, thereby improving gas sensing performances. As an electronic sensitization effect, the work function of the ZnO (3.77 eV) is lower than that of the Pd-Au alloy core (4.13 eV), so that electrons in ZnO shell are injected into Pd-Au alloy core in air (Fig. 9 and S10a). As a result, the baseline resistance in air (R_a) of Pd-Au_{NR}@ZnO CS-NPs sensor (92 MOhm) is increased by 48 times compared with pure ZnO sensor (1.9 MOhm). Moreover, hydrogen gas can easily reach the Pd-Au alloy core's surface because of the small kinetic diameter of the molecule and the ability of Pd-Au alloy core to absorb hydrogen and decompose into hydrogen atoms (H). The hydrogen atoms migrate to the ZnO surface to combine with O^- species at 250°C to produce water, and the released electrons return to the sensing materials, further decreasing the resistance R_g.

$$H_2 \rightarrow 2H \quad (6)$$

$$2H + O^- \rightarrow H_2O + e^- \quad (7)$$

Also, the Pd-Au alloy core can combine with the dissociated hydrogen atoms to form Pd-$Au_{NR}H_x$. The work function of the ZnO (3.77 eV) is larger than that of the Pd-$Au_{NR}H_x$ (1.38 eV) (Fig. S10). Therefore, the electrons transfer from the Pd-$Au_{NR}H_x$ to the ZnO (Fig. 9), which contributes to significantly reducing the resistance R_g of sensor, which then improves overall gas sensing performance.

$$Pd\text{-}Au_{NR} + xH \rightarrow Pd\text{-}Au_{NR}H_x \quad (8)$$

4. Conclusion

To investigate the effect of Pd-Au nanorod (NR) on the hydrogen gas sensing performances, three types of materials, including pure ZnO NPs, Au_{NR}@ZnO CS-NPs, and Pd-Au_{NR}@ZnO CS-NPs, were successfully synthesized by hydrothermal method, and efficient hydrogen detection was achieved. The highest response of pure ZnO, Au_{NR}@ZnO, and Pd-Au_{NR}@ZnO sensors were 13 at 350°C, 52, and 105 at 250°C for 100 ppm of hydrogen gas, respectively. The Pd-Au_{NR}@ZnO sensor's response was 8 times higher than that of pristine ZnO sensor because the baseline of electrical resistance in air (R_a) of the Pd-Au_{NR}@ZnO sensor was significantly greater than that of the pristine ZnO sensor. In addition, the Pd-Au_{NR}@ZnO sensor could detect at least 1 ppm of hydrogen gas even at low temperature (150°C). Moreover, the Pd-Au_{NR}@ZnO sensor showed excellent selectivity for hydrogen gas compared to other gases such as CH_3CHO, C_2H_5OH, CH_4, and CO. At a concentration of 100 ppm, the Pd-Au_{NR}@ZnO sensor's response to hydrogen gas was 24 times greater than its response to CO. The improved response and selectivity of the Pd-Au_{NR}@ZnO sensor were driven by the synergistic effect of the core morphology, electronic sensitization, and hydrogen absorption properties of the nanorod-shaped Pd-Au alloy core in the Pd-Au_{NR}@ZnO CS-NPs. That is, the large interface area between the ZnO shell and the nanorod-shaped Pd-Au core increased the baseline resistance R_a of Pd-Au_{NR}@ZnO CS-NPs due to the larger work function of Pd-Au alloy core, and further enhanced the adsorption amount of hydrogen gas. This demonstrated that the morphology of the Pd-Au alloy core played an important role in enhancing gas sensing performances. This work could open a new direction for designing more efficient hydrogen sensors.

CRediT authorship contribution statement

Dong-Seog Kim: Software, Formal analysis. **Geun-Jae Oh:** Software, Formal analysis. **Ho-Geun Song:** Investigation, Formal analysis. **Dae-Hee Won:** Writing – review & editing. **Yeon-Tae Yu:** Writing – review & editing, Visualization, Supervision, Project administration, Funding acquisition, Conceptualization. **Tuong Van Tran:** Writing – original draft, Software, Resources, Methodology, Investigation, Formal analysis, Data curation, Conceptualization.

Declaration of Competing Interest

The authors declare that they have no known competing financial interests or personal relationships that could have appeared to influence the work reported in this paper.

Acknowledgements

This work was supported by 1) the BK21-FOUR program of the Ministry of Education and Human-Resource Development, South Korea; and 2) the National Research Foundation of Korea (NRF) and the Commercialization Promotion Agency for R&D Outcomes (COMPA) grant funded by the Korea government (Ministry of Science and ICT) (RS-2025-02314407). 3) The Regional Innovation System & Education (RISE) initiative, funded by the Ministry of Education and administered by the National Research Foundation of Korea (NRF).

Appendix A. Supporting information

Supplementary data associated with this article can be found in the online version at doi:10.1016/j.snb.2025.138210.

Data availability

Data will be made available on request.

References

[1] Y.S.H. Najjar, Hydrogen safety: the road toward green technology, Int. J. Hydrog. Energy 38 (2013) 10716–10728, https://doi.org/10.1016/j.ijhydene.2013.05.126.
[2] Q. Hassan, A.Z. Sameen, O. Olapade, M. Alghoul, H.M. Salman, M. Jaszczur, Hydrogen fuel as an important element of the energy storage needs for future smart cities, Int. J. Hydrog. Energy 48 (2023) 30247–30262, https://doi.org/10.1016/j.ijhydene.2023.03.413.
[3] T.S. Uyar, D. Beşikci, Integration of hydrogen energy systems into renewable energy systems for better design of 100% renewable energy communities, Int. J. Hydrog. Energy 42 (2017) 2453–2456, https://doi.org/10.1016/j.ijhydene.2016.09.086.
[4] Y.S. Shim, L. Zhang, D.H. Kim, Y.H. Kim, Y.R. Choi, S.H. Nahm, C.Y. Kang, W. Lee, H.W. Jang, Highly sensitive and selective H2 and NO2 gas sensors based on surface-decorated WO3 nanoigloos, Sens. Actuators B Chem. 198 (2014) 294–301, https://doi.org/10.1016/j.snb.2014.03.073.
[5] B. Liu, D. Cai, Y. Liu, D. Wang, L. Wang, Y. Wang, H. Li, Q. Li, T. Wang, Improved room-temperature hydrogen sensing performance of directly formed Pd/WO3 nanocomposite, Sens. Actuators B Chem. 193 (2014) 28–34, https://doi.org/10.1016/j.snb.2013.11.057.
[6] S. Dutta, A review on production, storage of hydrogen and its utilization as an energy resource, J. Ind. Eng. Chem. 20 (2014) 1148–1156, https://doi.org/10.1016/j.jiec.2013.07.037.
[7] T. Hübert, L. Boon-Brett, G. Black, U. Banach, Hydrogen sensors - A review, Sens. Actuators B Chem. 157 (2011) 329–352, https://doi.org/10.1016/j.snb.2011.04.070.
[8] G.A. Karim, Hydrogen as a spark ignition engine fuel, Q. 8, Chem. Ind. Chem. Eng. (2002) 256–263, https://doi.org/10.2298/hemind0206256k.
[9] J.G. Firth, A. Jones, T.A. Jones, The principles of the detection of flammable atmospheres by catalytic devices, Combust. Flame 20 (1973) 303–311, https://doi.org/10.1016/0010-2180(73)90021-7.
[10] Y.K. Gautam, K. Sharma, S. Tyagi, A.K. Ambedkar, M. Chaudhary, B. Pal Singh, Nanostructured metal oxide semiconductor-based sensors for greenhouse gas detection: progress and challenges, R. Soc. Open Sci. 8 (2021), https://doi.org/10.1098/rsos.201324.
[11] M.Z. Atashbar, G. Korotcenkov, S. Krishnamurthy, Basic principles of chemical sensors operation B, Chem. Sens. Fundam. Sens. Mater. (2009). ⟨https://www.researchgate.net/publication/286451678⟩.
[12] Q. Liang, Y. Guo, H. Chen, M.H. Fan, N. Bai, X. Zou, G.D. Li, Energy level regulation to optimize hydrogen sensing performance of porous bimetallic gallium-indium oxide with ultrathin pore walls, Sens. Actuators B Chem. 350 (2022) 130864, https://doi.org/10.1016/j.snb.2021.130864.
[13] M.V. Nikolic, V. Milovanovic, Z.Z. Vasiljevic, Z. Stamenkovic, Semiconductor gas sensors: materials, technology, design, and application, Sensors 20 (2020) 1–31, https://doi.org/10.3390/s20226694.
[14] M. Dadkhah, J.M. Tulliani, Green synthesis of metal oxides semiconductors for gas sensing applications, Sensors 22 (2022), https://doi.org/10.3390/s22134669.
[15] L. Boon-Brett, J. Bousek, G. Black, P. Moretto, P. Castello, T. Hübert, U. Banach, Identifying performance gaps in hydrogen safety sensor technology for automotive and stationary applications, Int. J. Hydrog. Energy 35 (2010) 373–384, https://doi.org/10.1016/j.ijhydene.2009.10.064.
[16] V. Aroutiounian, Metal oxide hydrogen, oxygen, and carbon monoxide sensors for hydrogen setups and cells, Int. J. Hydrog. Energy 32 (2007) 1145–1158, https://doi.org/10.1016/j.ijhydene.2007.01.004.
[17] Q. Ren, Y.-Q. Cao, D. Arulraj, C. Liu, D. Wu, W.-M. Li, A.-D. Li, Review—resistive-type hydrogen sensors based on zinc oxide nanostructures, J. Electrochem. Soc. 167 (2020) 067528, https://doi.org/10.1149/1945-7111/ab7e23.
[18] J.Le Xie, C.X. Guo, C.M. Li, Construction of one-dimensional nanostructures on graphene for efficient energy conversion and storage, Energy Environ. Sci. 7 (2014) 2559–2579, https://doi.org/10.1039/c4ee00531g.
[19] T.T.D. Nguyen, D.Van Dao, D.S. Kim, H.J. Lee, S.Y. Oh, I.H. Lee, Y.T. Yu, Effect of core and surface area toward hydrogen gas sensing performance using Pd@ZnO core-shell nanoparticles, J. Colloid Interface Sci. 587 (2021) 252–259, https://doi.org/10.1016/j.jcis.2020.12.017.
[20] Y. Zhang, K. Yu, D. Jiang, Z. Zhu, H. Geng, L. Luo, Zinc oxide nanorod and nanowire for humidity sensor, Appl. Surf. Sci. 242 (2005) 212–217, https://doi.org/10.1016/j.apsusc.2004.08.013.
[21] J.J. Hassan, M.A. Mahdi, C.W. Chin, H. Abu-Hassan, Z. Hassan, A high-sensitivity room-temperature hydrogen gas sensor based on oblique and vertical ZnO nanorod arrays, Sens. Actuators B Chem. 176 (2013) 360–367, https://doi.org/10.1016/j.snb.2012.09.081.
[22] P. Rai, S.H. Jeon, C.H. Lee, J.H. Lee, Y.T. Yu, Functionalization of ZnO nanorods by CuO nanospikes for gas sensor applications, RSC Adv. 4 (2014) 23604–23609, https://doi.org/10.1039/c4ra00078a.
[23] S. Chaudhary, A. Umar, K.K. Bhasin, S. Baskoutas, Chemical sensing applications of ZnO nanomaterials, Materials 11 (2018) 1–38, https://doi.org/10.3390/ma11020287.
[24] M. Que, C. Lin, J. Sun, L. Chen, X. Sun, Y. Sun, Progress in zno nanosensors, Sensors 21 (2021) 1–22, https://doi.org/10.3390/s21165502.
[25] Z.U. Abideen, J.H. Kim, J.H. Lee, J.Y. Kim, A. Mirzaei, H.W. Kim, S.S. Kim, Electrospun metal oxide composite nanofibers gas sensors: a review, J. Korean Ceram. Soc. 54 (2017) 366–379, https://doi.org/10.4191/kcers.2017.54.5.12.
[26] T.T.D. Nguyen, D. Van Dao, N. Thi Thu Ha, T. Van Tran, D.S. Kim, J.W. Yoon, N. N. Ha, I.H. Lee, Y.T. Yu, Superhigh sensing response and selectivity for hydrogen gas using PdPt@ZnO core-shell nanoparticles: unique effect of alloyed ingredient from experimental and theoretical investigations, Sens. Actuators B Chem. 354 (2022) 131083, https://doi.org/10.1016/j.snb.2021.131083.
[27] A. Mirzaei, S.G. Leonardi, G. Neri, Detection of hazardous volatile organic compounds (VOCs) by metal oxide nanostructures-based gas sensors: a review, Ceram. Int. 42 (2016) 15119–15141, https://doi.org/10.1016/j.ceramint.2016.06.145.
[28] Y. Kang, F. Yu, L. Zhang, W. Wang, L. Chen, Y. Li, Review of ZnO-based nanomaterials in gas sensors, Solid State Ion. 360 (2021) 115544, https://doi.org/10.1016/j.ssi.2020.115544.
[29] M. Khanuja, S. Kala, B.R. Mehta, F.E. Kruis, Concentration-specific hydrogen sensing behavior in monosized Pd nanoparticle layers, Nanotechnology 20 (2009), https://doi.org/10.1088/0957-4484/20/1/015502.
[30] B.D. Adams, A. Chen, The role of palladium in a hydrogen economy, Mater. Today 14 (2011) 282–289, https://doi.org/10.1016/S1369-7021(11)70143-2.
[31] Q. Li, L. Wang, A. Xiao, L. Zhu, Z. Yang, Hydrogen sensing towards palladium-based nanocomposites: a review, Int. J. Hydrog. Energy (2024), https://doi.org/10.1016/j.ijhydene.2024.01.001.
[32] W. Kim, B. Jang, H.S. Lee, W. Lee, Reliability and selectivity of H2 sensors composed of Pd Film nanogaps on an elastomeric substrate, Sens. Actuators B Chem. 224 (2016) 547–551, https://doi.org/10.1016/j.snb.2015.10.092.
[33] A. Mirzaei, H.R. Yousefi, F. Falsafi, M. Bonyani, J.H. Lee, J.H. Kim, H.W. Kim, S. S. Kim, An overview on how Pd on resistive-based nanomaterial gas sensors can enhance response toward hydrogen gas, Int. J. Hydrog. Energy 44 (2019) 20552–20571, https://doi.org/10.1016/j.ijhydene.2019.05.180.
[34] J. Van Lith, A. Lassesson, S.A. Brown, M. Schulze, J.G. Partridge, A. Ayesh, A hydrogen sensor based on tunneling between palladium clusters, Appl. Phys. Lett. 91 (2007) 1–4, https://doi.org/10.1063/1.2802730.
[35] D.S. Selishchev, N.S. Kolobov, A.V. Bukhtiyarov, E.Y. Gerasimov, A.I. Gubanov, D. V. Kozlov, Deposition of Pd nanoparticles on TiO2 using a Pd(acac)2 precursor for photocatalytic oxidation of CO under UV-LED irradiation, Appl. Catal. B Environ. 235 (2018) 214–224, https://doi.org/10.1016/j.apcatb.2018.04.074.
[36] J.Y. Kim, J.H. Lee, J.H. Kim, A. Mirzaei, H. Woo Kim, S.S. Kim, Realization of H2S sensing by Pd-functionalized networked CuO nanowires in self-heating mode, Sens. Actuators B Chem. 299 (2019) 126965, https://doi.org/10.1016/j.snb.2019.126965.
[37] M. Lyubovsky, L. Pfefferle, Methane combustion over the α-alumina supported Pd catalyst: activity of the mixed Pd/PdO state, Appl. Catal. A Gen. 173 (1998) 107–119, https://doi.org/10.1016/S0926-860X(98)00149-5.
[38] D. Zhang, C. Jin, H. Tian, Y. Xiong, H. Zhang, P. Qiao, J. Fan, Z. Zhang, Z.Y. Li, J. Li, An: In situ TEM study of the surface oxidation of palladium nanocrystals assisted by electron irradiation, Nanoscale 9 (2017) 6327–6333, https://doi.org/10.1039/c6nr08763a.
[39] C. Liewhiran, N. Tamaekong, A. Wisitsoraat, A. Tuantranont, S. Phanichphant, Ultra-sensitive H2+ sensors based on flame-spray-made Pd-loaded SnO2+ sensing films, Sens. Actuators B Chem. 176 (2013) 893–905, https://doi.org/10.1016/j.snb.2012.10.087.
[40] T. Van Tran, D.S. Kim, T. Duc Le, G.J. Oh, G.S. Shin, Y.T. Yu, Alloy core composition effect of Pd-Augr-alloy@ZnO core–shell nanoparticles on hydrogen gas sensing performance, Chem. Eng. J. 483 (2024) 149050, https://doi.org/10.1016/j.cej.2024.149050.
[41] J.M. Rahm, J. Löfgren, E. Fransson, P. Erhart, A tale of two phase diagrams: interplay of ordering and hydrogen uptake in Pd–Au–H, Acta Mater. 211 (2021) 116893, https://doi.org/10.1016/j.actamat.2021.116893.
[42] R.J. Westerwaal, J.S.A. Rooijmans, L. Leclercq, D.G. Gheorghe, T. Radeva, L. Mooij, T. Mak, L. Polak, M. Slaman, B. Dam, T. Rasing, Nanostructured Pd-Au based fiber optic sensors for probing hydrogen concentrations in gas mixtures, Int. J. Hydrog. Energy 38 (2013) 4201–4212, https://doi.org/10.1016/j.ijhydene.2012.12.146.

[43] H. Deepti, A. Kumar, A.B. Tripathi, M. Dey, R. Gupta, D.K. Krishna, Avasthi, Improved hydrogen sensing behaviour in ion-irradiated Pd-Au alloy thin films, Sens. Actuators B Chem. 301 (2019) 127006, https://doi.org/10.1016/j.snb.2019.127006.
[44] T. Van Tran, M.J. Ahemad, D.S. Kim, T.D. Le, V. Dao, Y.T. Yu, Ultra high response for hydrogen gas on Pd–Augr-alloy@ZnO core-shell nanoparticles with Pd–Au gradient composition alloy core, Mater. Today Nano 21 (2023), https://doi.org/10.1016/j.mtnano.2022.100292.
[45] X. Lu, L. Tao, D. Song, Y. Li, F. Gao, Bimetallic Pd@Au nanorods based ultrasensitive acetylcholinesterase biosensor for determination of organophosphate pesticides, Sens. Actuators B Chem. 255 (2018) 2575–2581, https://doi.org/10.1016/j.snb.2017.09.063.
[46] P. Rai, Y.T. Yu, Potential barrier modulation in ZnO nanostructures and their CO sensing properties, Anal. Methods 5 (2013) 4081–4087, https://doi.org/10.1039/c3ay40245b.
[47] J. Tamaki, A. Miyaji, J. Makinodan, S. Ogura, S. Konishi, Effect of micro-gap electrode on detection of dilute NO2 using WO3 thin film microsensors, Sens. Actuators B Chem. 108 (2005) 202–206, https://doi.org/10.1016/j.snb.2004.09.047.
[48] P. Rai, R. Khan, S. Raj, S.M. Majhi, K.K. Park, Y.T. Yu, I.H. Lee, P.K. Sekhar, Au@Cu2O core-shell nanoparticles as chemiresistors for gas sensor applications: effect of potential barrier modulation on the sensing performance, Nanoscale 6 (2014) 581–588, https://doi.org/10.1039/c3nr04118b.
[49] P. Rai, W.K. Kwak, Y.T. Yu, Solvothermal synthesis of ZnO nanostructures and their morphology-dependent gas-sensing properties, ACS Appl. Mater. Interfaces 5 (2013) 3026–3032, https://doi.org/10.1021/am302811h.
[50] R.W.J. Scott, S.M. Yang, G. Chabanis, N. Coombs, D.E. Williams, G.A. Ozin, Tin dioxide opals and inverted opals: near-ideal microstructures for gas sensors, Adv. Mater. 13 (2001) 1468–1472, https://doi.org/10.1002/1521-4095(200110)13:19<1468::AID-ADMA1468>3.0.CO;2-O.
[51] Y. Zhang, T. Han, Z. Wang, C. Zhao, J. Li, T. Fei, S. Liu, G. Lu, T. Zhang, In situ formation of N-doped carbon film-immobilized Au nanoparticles-coated ZnO jungle on indium tin oxide electrode for excellent high-performance detection of hydrazine, Sens. Actuators B Chem. 243 (2017) 1231–1239, https://doi.org/10.1016/j.snb.2016.12.085.
[52] S. Wang, X. Wang, G. Qiao, X. Chen, X. Wang, H. Cui, Core-double shell ZnO@In2O3@ZnO hollow microspheres for superior ethanol gas sensing, Sens. Actuators B Chem. 341 (2021) 130002, https://doi.org/10.1016/j.snb.2021.130002.
[53] S.M. Majhi, H.J. Lee, H.N. Choi, H.Y. Cho, J.S. Kim, C.R. Lee, Y.T. Yu, Construction of novel hybrid PdO-ZnO p-n heterojunction nanostructures as a high-response sensor for acetaldehyde gas, CrystEngComm 21 (2019) 5084–5094, https://doi.org/10.1039/c9ce00710e.
[54] M.J. Ahemad, T.D. Le, D.S. Kim, Y.T. Yu, Bimetallic AgAualloy@ZnO core-shell nanoparticles for ultra-high detection of ethanol: potential impact of alloy composition on sensing performance, Sens. Actuators B Chem. 359 (2022) 131595, https://doi.org/10.1016/j.snb.2022.131595.
[55] M.J. Ahemad, D.S. Kim, T. Duc Le, L.R. Nagappagari, G.J. Oh, G.S. Shin, U. Ahmad, S.A. Akbar, Y.T. Yu, Thermally stable AgPd@ZnO bimetallic alloy nanoparticles for ethanol sensors with long-term stability, ACS Appl. Nano Mater. 5 (2022) 18568–18580, https://doi.org/10.1021/acsanm.2c04380.
[56] J. Park, P.R. Deshmukh, Y. Sohn, W.G. Shin, ZnO-TiO2 core-shell nanowires decorated with Au nanoparticles for plasmon-enhanced photoelectrochemical water splitting, J. Alloy. Compd. 787 (2019) 1310–1319, https://doi.org/10.1016/j.jallcom.2019.02.061.
[57] D. Ramírez-Ortega, D. Guerrero-Araque, P. Acevedo-Peña, E. Reguera, H. A. Calderon, R. Zanella, Enhancing the photocatalytic hydrogen production of the ZnO–TiO2 heterojunction by supporting nanoscale Au islands, Int. J. Hydrog. Energy 46 (2021) 34333–34343, https://doi.org/10.1016/j.ijhydene.2021.08.019.
[58] A. Bumajdad, M. Madkour, Y. Abdel-M1 am, M. El-Kemary, Nanostructured mesoporous Au/TiO2 for photocatalytic degradation of a textile dye: the effect of size similarity of the deposited Au with that of TiO2 pores, J. Mater. Sci. 49 (2014) 1743–1754, https://doi.org/10.1007/s10853-013-7861-0.
[59] Y. Cheng, S. Lu, W. Xu, H. Wen, J. Wang, Fabrication of superhydrophobic Au-Zn alloy surface on a zinc substrate for roll-down, self-cleaning and anti-corrosion properties, J. Mater. Chem. A. 3 (2015) 16774–16784, https://doi.org/10.1039/c5ta03979g.
[60] T. Sahm, A. Gurlo, N. Bârsan, U. Weimar, Basics of oxygen and SnO2 interaction; work function change and conductivity measurements, Sens. Actuators B Chem. 118 (2006) 78–83, https://doi.org/10.1016/j.snb.2006.04.004.
[61] A. Rossi, E. Spagnoli, A. Visonà, D. Ahmed, M. Marzocchi, V. Guidi, B. Fabbri, SO2 detection over a wide range of concentrations: an exploration on MOX-based gas sensors, Chemosensors 12 (2024), https://doi.org/10.3390/chemosensors12060111.

Tuong Van Tran received his Ph.D. degree in 2025 from Jeonbuk National University, South Korea. He is currently serving as a Postdoctoral Researcher at the Division of Advanced Materials Engineering, Jeonbuk National University. His research interests are in the synthesis of metal@oxide core-shell nanoparticles and their application for gas sensors.

Dong-Seog Kim is currently a Ph.D. candidate at the Division of Advanced Materials Engineering, Jeonbuk National University. He obtained his master's degree (MS) in 2022 from Jeonbuk National University. His research interests focus on synthesizing core-shell nanomaterials and their applications in chemical gas sensors.

Geun-Jae Oh is currently a Ph.D. student at the Division of Advanced Materials Engineering, Jeonbuk National University. His research interests are focused on the synthesis of core-shell nanomaterials and their applications in photocatalysis and chemical gas sensors.

Ho-Geun Song graduated from the Department of Chemical Engineering at Inha University in 1981 and received his master's degree from the Department of Inorganic Materials Engineering at Pusan National University in 1999. He joined LG Innotek in 1987 and worked there for 15 years. He founded Ogam Technology Co., Ltd., a gas sensor company, in 2000 and is currently the CEO.

Dae-Hee Won is an Associate Professor at the Graduate School of Liberal Arts and Sciences, Wonkwang University. He earned his bachelor's degree in Metallurgical Engineering from Jeonbuk National University in 1993, followed by a Ph.D. in Engineering from the same institution in 1999. From 2005–2012, he served as a professor at National Suncheon University. In 2014, he joined Wonkwang University as an Assistant Professor in the Department of Mechanical and Automotive Engineering, and in 2021, he transitioned to the Graduate School of Education. His research interests encompass nanomarterials design, biomaterials, biosensors, titanium surface treatment, and TRIZ (Theory of Inventive Problem Solving).

Yeon-Tae Yu (Professor) works for Jeonbuk National University, Division of Advanced Materials Engineering. In 1988, he obtained his engineering diploma in the Department of Metallurgy Engineering from Jeonbuk National University in South Korea, and in 1993, he received his doctorate from Tohoku University, Japan. He worked at the Korea Institute of Geoscience and Mineral Resources as a senior researcher from 1993 until 2003. He became a professor at Jeonbuk National University's Division of Advanced Materials Engineering in 2004. His main research interests include the synthesis of composite nanoparticles with a core-shell structure and their use as fuel-cell, photocatalysts, and gas sensors.